AGU PUBLICATIONS

JGR

Journal of Geophysical Research: Space Physics

RESEARCH ARTICLE
10.1002/2016JA022913

Key Points:
- Source regions of Saturn 5 kHz *Z*-mode emission are located
- Wave amplitude and electron PSD are analyzed
- Temperature anisotropy and quasi-steady conditions near Enceladus torus drive *Z* mode

Correspondence to:
J. D. Menietti,
john-menietti@uiowa.edu

Citation:
Menietti, J. D., P. H. Yoon, D. Písa, S.-Y. Ye, O. Santolík, C. S. Arridge, D. A. Gurnett, and A. J. Coates (2016), Source region and growth analysis of narrowband *Z*-mode emission at Saturn, *J. Geophys. Res. Space Physics*, *121*, 11,929–11,942, doi:10.1002/2016JA022913.

Received 5 MAY 2016
Accepted 18 NOV 2016
Accepted article online 20 NOV 2016
Published online 22 DEC 2016

Source region and growth analysis of narrowband *Z*-mode emission at Saturn

J. D. Menietti[1], P. H. Yoon[2,3], D. Písa[1,4], S.-Y. Ye[1], O. Santolík[4,5], C. S. Arridge[6], D. A. Gurnett[1], and A. J. Coates[7]

[1]Department of Physics and Astronomy, University of Iowa, Iowa City, Iowa, USA, [2]Institute for Physical Science and Technology, University of Maryland, College Park, Maryland, USA, [3]School of Space Research, Kyung Hee University, Yongin, South Korea, [4]Institute of Atmospheric Physics ASCR, Prague, Czech Republic, [5]Faculty of Mathematics and Physics, Charles University, Prague, Czech Republic, [6]Department of Physics, Lancaster University, Lancaster, UK, [7]Mullard Space Science Laboratory, University College London, Dorking Surrey, UK

Abstract Intense *Z*-mode emission is observed in the lower density region near the inner edge of the Enceladus torus at Saturn, where these waves may resonate with MeV electrons. The source mechanism of this emission, which is narrow-banded and most intense near 5 kHz, is not well understood. We survey the Cassini Radio and Plasma Wave Science data to isolate several probable source regions near the inner edge of the Enceladus density torus. Electron phase space distributions are obtained from the Cassini Electron Spectrometer, part of the Cassini Plasma Spectrometer investigation. We perform a plasma wave growth analysis to conclude that an electron temperature anisotropy and possibly a weak loss cone can drive the *Z* mode as observed. Electrostatic electron acoustic waves and perhaps weak beam modes are also found to be unstable coincident with the *Z* mode. Quasi-steady conditions near the Enceladus density torus may result in the observations of narrowband *Z*-mode emission at Saturn.

1. Introduction

Z-mode radio emission is observed at Earth in the auroral regions [*Gurnett et al*., 1983] and in the plasmapause associated with upper hybrid emissions [*Kurth*, 1982; *Menietti and Yoon*, 2006]. The emission propagates in the frequency range $f_z < f < f_{uh}$, where $f_Z = \frac{1}{2}\left(\sqrt{f_{ce}^2 + 4f_{pe}^2} - f_{ce}\right)$ (cutoff frequency) and $f_{uh} = \sqrt{{f_{ce}}^2 + {f_{pe}}^2}$ (upper hybrid resonance) with f_{ce} and f_{pe} as the cyclotron frequency and plasma frequency, respectively. Thus, the frequency range can overlap whistler mode, but with different polarization. As discussed, for example, in *Benson et al*. [2006], for *Z*-mode frequencies $f/f_{pe} < 1$, *Z* mode is left-hand polarized, while for $f/f_{pe} > 1$, it is right-hand polarized. In addition, the indices of refraction of the whistler mode and *Z* mode can overlap near f_{pe} for the condition $f_{pe}/f_{ce} < 1$ as shown in Figure 4.38 of *Gurnett and Bhattacharjee* [2005].

Z-mode emissions can play an important role in the acceleration of electrons in a similar manner as the whistler mode. Both wave modes can contribute to diffusive scattering of electrons [cf. *Horne and Thorne*, 1998; *Glauert and Horne*, 2005; *Albert*, 2007; *Xiao et al*., 2012]. In particular, *Gu et al*. [2013] have shown that *Z*-mode waves at Saturn may be responsible for local acceleration of electrons from hundreds of keV to tens of MeV at intermediate pitch angles. Thus, *Z* mode may supplement chorus emission as a possible significant source of electron acceleration filling the radiation zones at Saturn [*Shprits et al*., 2012; *Menietti et al*., 2014, 2015].

Ye et al. [2010] have shown that narrowband 5 kHz emission at Saturn frequently propagates in the *Z* mode, with the most intense observations occurring in the low-density regions inside the orbit of Enceladus, where $f_{pe}/f_{ce} < 1$. *Ye et al*. [2010] have proposed that Saturn 5 kHz *Z*-mode emission may have an auroral source region. The discovery that this emission shows a rotation periodicity that is the same as Saturn kilometric radiation (SKR) also strongly supports an auroral source region. *Menietti et al*. [2011] subsequently analyzed SKR near a source region and indicated that the observed electron phase space distribution supports the wave growth of locally observed extraordinary, ordinary, and *Z*-mode emissions. The present study does not dispute any of these findings. However, we present here evidence that *Z* mode may also have a source near the equator where the most intense emissions are observed. *Menietti et al*. [2015] surveyed Saturn's inner magnetosphere for *Z*-mode intensity as a function of frequency and position. In the current study we

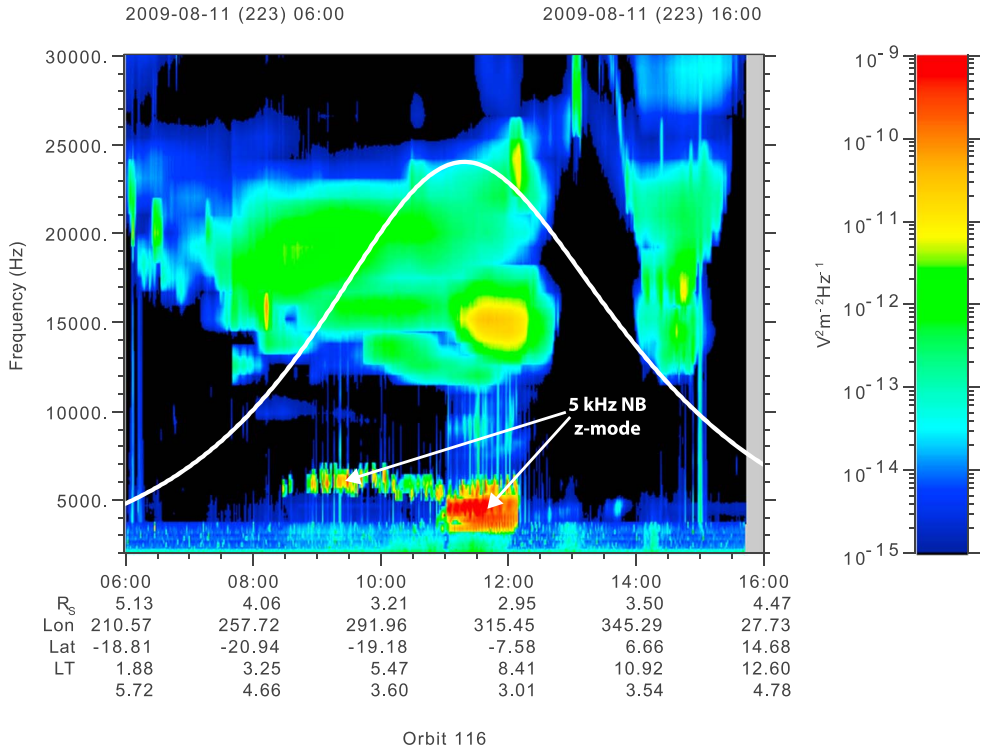

Figure 1. A spectrogram of *Z*-mode emission for day 223 of 2008, indicative of a probable source region. This emission is intense, narrow-banded centered near 5 kHz, $\omega < \Omega_{ce}$. Note that the intense *Z* mode (~11:00 to ~12:15) is also coincident with intense, broad-banded electrostatic emission (green color). The white line is the electron cyclotron frequency.

present results of a search of probable sources of *Z* mode in this region. Electron phase space data from the Cassini Plasma Spectrometer (CAPS) Electron Spectrometer (ELS) [*Young et al.*, 2004; *Coates et al.*, 1996; *Arridge et al.*, 2009] are used to model the expected growth rate of waves in one probable source region.

2. *Z*-mode Observations

A survey of Cassini Radio and Plasma Wave Science investigation (RPWS) [*Gurnett et al.*, 2004] data revealed at least a half dozen examples of intense *Z*-mode emission in the inner Saturn magnetosphere that are candidates for source regions. All of the regions occur approximately 15 to 35° away from the magnetic equator and near the inner edge of the density torus where $f_{pe}/f_{ce} < 1$. In Figure 1 we display a spectrogram of *Z*-mode emission for day 223 of 2008 that is characteristic of what we believe to be a probable source region. This emission is seen to be narrow-banded centered near 5 kHz at frequencies and well below the cyclotron frequency, f_{ce}. This pass was discussed in some detail in *Menietti et al.* [2015], but no electron phase space distribution (PSD) was available for wave growth analysis. As the spacecraft approaches the equator with increasing density and cyclotron frequency, the emission becomes quite intense for times in the range of ~11:00 to ~12:15 and is close to the anticipated source region. Note also the intense broadband electrostatic emission coincident in time and overlapping in frequency with the intense *Z* mode. This emission is seen weakly on spectrograms of the magnetic spectral density.

In order to conduct an analysis of wave growth it is necessary to obtain the electron phase space distribution in the emission source region, which may be obtained from the Electron Spectrometer (ELS), one of three sensors of the Cassini Plasma Spectrometer (CAPS). The ELS sensor is an electrostatic analyzer with a fan-shaped array of eight anodes (detectors) that operate in an energy range from 0.6 eV to ~28 keV. Each anode has a field of view of approximately 20° with some overlap.

In Table 1 we list some of the better examples of probable source regions of *Z*-mode emission. Of the six cases studied, only day 168 of 2008 provided minimally sufficient coverage of phase space from

Table 1. Probable *Z*-Mode (5 kHz) Source Regions

		Northern		Southern	
Year	Day of Year	Start	Stop	Start	Stop
2008	168	03:20	04:30		
2008	182	07:30	08:10	09:15	10:10
2008	196	09:00	09:55	10:45	11:50
2008	203	10:15	10:50	11:40	12:30
2009	223			11:00	12:10
2010	027	05:00	06:30		

nonobstructed ELS anodes. Obstruction occurs as a result of an anode being partially or completely blocked by the Cassini spacecraft from plasma flux or perhaps susceptible to electron flux scattered by the spacecraft into the anode. The orientation of the spacecraft is important in determining which anodes may be obstructed. The *Z*-mode emission observed on days 167 and 168 in 2008 is shown in Figure 2a, centered near 5 kHz with the most intense emission observed at lower latitudes. The Cassini spacecraft during this time is in a high inclination orbit and travels from high northern to high southern latitudes crossing the magnetic equator near 04:50 on day 168. The plasma density is higher adjacent to the magnetic equator, where the most intense emission is observed. The white line is the local electron cyclotron frequency calculated from the fluxgate magnetometer measurements [*Dougherty et al*., 2004]. In Figure 2b we show a higher-resolution plot with linear frequency scale of the most intense emission centered near a frequency of 5 kHz. The white dots are approximately 1 min averages of the plasma frequency obtained from the Langmuir Probe instrument (part of the RPWS) onboard Cassini [*Wahlund et al*., 2005]. No data are available beyond ~04:12, after which the density increases as the magnetic equator and ring plane are approached [*Persoon et al*., 2013]. The narrow in time, intense, broadband emission near 04:50 is the signature of the ring plane crossing at the magnetic equator. This particular magnetic equator crossing was studied in more detail by *Gu et al*. [2013] as mentioned in section 1. Electron phase space density (PSD) as a function of time during the intense 5 kHz emission is shown in Figure 3. All eight anodes of ELS are plotted, with the pitch angle (α) of each anode plotted in the bottom plot. The pattern is similar for each anode, with a decrease in electron PSD for pitch angles near 0°, and a slow increase in peak energy as a function of time. The ELS instrument during this time period collected data for all anodes every 4 s. However, because of the orientation of the spacecraft during this period, the time required to obtain the full range of pitch angles (0 to 180°) is approximately 3.5 min.

To analyze these data we have therefore singled out two periods of time, the first when the anodes are monitoring pitch angles closer to the anti-field-aligned direction, which we call Set A ($\alpha > 90°$, 03:31:59 to 03:32:01), and the second when the anodes sample pitch angles centered nearer the field-aligned direction, which we call Set B ($\alpha < 90°$, 03:35:43 to 03:35:45). We have combined both data sets, after eliminating partially obstructed anodes. The pitch angles for this analysis were obtained by using the magnetic field orientation [*Dougherty et al*., 2004] and the Cassini ELS instrument anode directions [*Young et al*., 2004]. The location of the spacecraft for the time periods discussed in this investigation is near magnetic field lines connected to Saturn's radiation belts, and saturation of the ELS detectors occurs at times, but not during the times of our data set. For our analyses we have included two anodes nearest the anti-field-aligned direction, which are partially obstructed (centered near $\alpha = 167°$ and $\alpha = 168°$). These anodes show similar fluxes to the adjacent anode ($\alpha = 154°$). Without these anodes, we have insufficient data near the anti-field-aligned direction to obtain a converging least squares fit to the data. We have also eliminated two nonobstructed anodes from Set B (centerline pitch angles of 107° and 127°) that overlap in pitch angle coverage of Set A. Sampling of electron flux for Set A is generally larger than for Set B as we noted above (Figure 3), and we avoid any additional differences due to the time delay between the sampling of Set A and Set B by eliminating any overlapping anode coverage between the two sets. No other nonobstructed anodes overlapped in coverage. A list of the anodes included in the study is given in Table 2. The resulting distribution (after mirroring the data about the $v_{\|}$ axis) is displayed in Figure 4a.

There are two obvious characteristics of these data. First, there is a distinct increase in electron phase space density in the anti-field-aligned direction (also seen in Figure 3), and second, there is a temperature

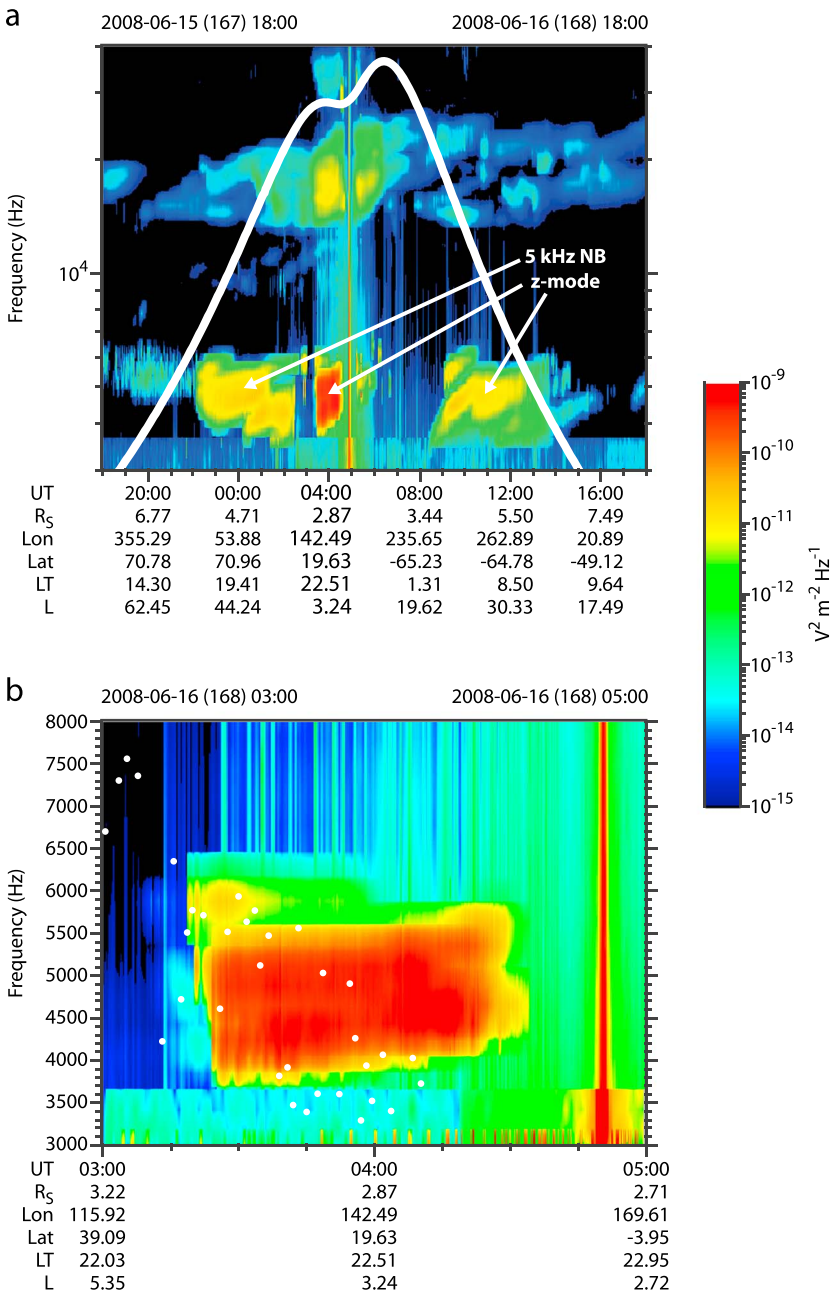

Figure 2. (a) Narrowband *Z*-mode emission observed on days 167 and 168 in 2008, centered near 5 kHz with the most intense emission observed at lower latitudes as the density increases and broadband electrostatic emission becomes intense (~03:00–04:30). The white line is the cyclotron frequency. (b) A higher-resolution plot of the most intense emission centered near 5 kHz. The intense, narrow in time, broadband emission near 04:50 is the signature of the ring plane crossing near the magnetic equator. The white dots are ~1 min averages of the plasma frequency obtained from the Langmuir Probe.

anisotropy (also for the anti-field-aligned direction). We have performed a nonlinear least squares fit of these data to a combination of five bi-Maxwellians ($w_\parallel$ and $w_\perp$ are the parallel and perpendicular thermal speeds),

$$f = \sum_{s=1}^{m} f_s,$$
$$f_s = \frac{n_s}{\pi^{3/2} w_{\perp s}^2 w_{\parallel s}} \exp\left(-\frac{v_\perp^2}{w_{\perp s}^2} - \frac{(v_\parallel - v_{ds})^2}{w^2{}_{\parallel s}} \right). \quad (1)$$

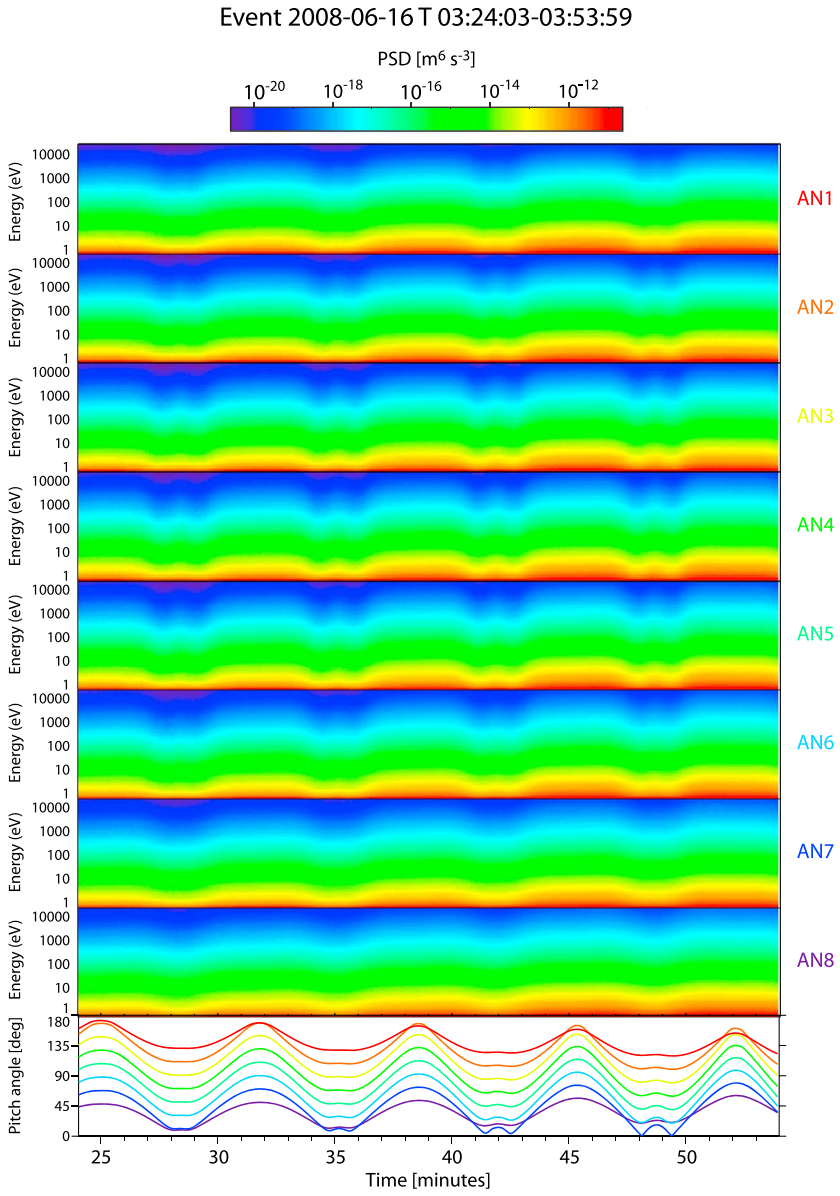

Figure 3. Electron phase space density (PSD) as a function of time during the intense emission shown in Figure 3. All eight anode of ELS are plotted, with the pitch angle (α) of each anode in the bottom plot. The pattern is similar for each anode, showing a decrease in electron PSD for pitch angles near 0°, and a slow increase in overall peak energy as a function of time. The time axis units are in minutes after the start time (3 h 24 min 3 s).

The variable fit parameters are n, w, and $T_{\perp}/T_{||}$ for each population. The fitting routine uses a gradient-expansion algorithm [cf. *Bevington*, 1969] to compute a nonlinear least squares fit to a user-supplied function with known partial derivatives. The goodness-of-fit statistic, χ^2, is weighted by the standard deviation. We initially started with three plasma populations ($m = 3$ in equation (1)), but we increased this number to 5 to obtain correspondingly better fits. For the values of $m = 3$, 4, and 5 populations the corresponding fits yielded

Table 2. Selected ELS Anode Centerline Pitch Angle (Deg) of Anodes

	H:Min:S	Deg	Deg	Deg	Deg	Deg
Set A	03:31:59	168[a]	167[a]	149	129	109
Set B	03:35:43	87	67	47	27	8

[a]Partially obstructed.

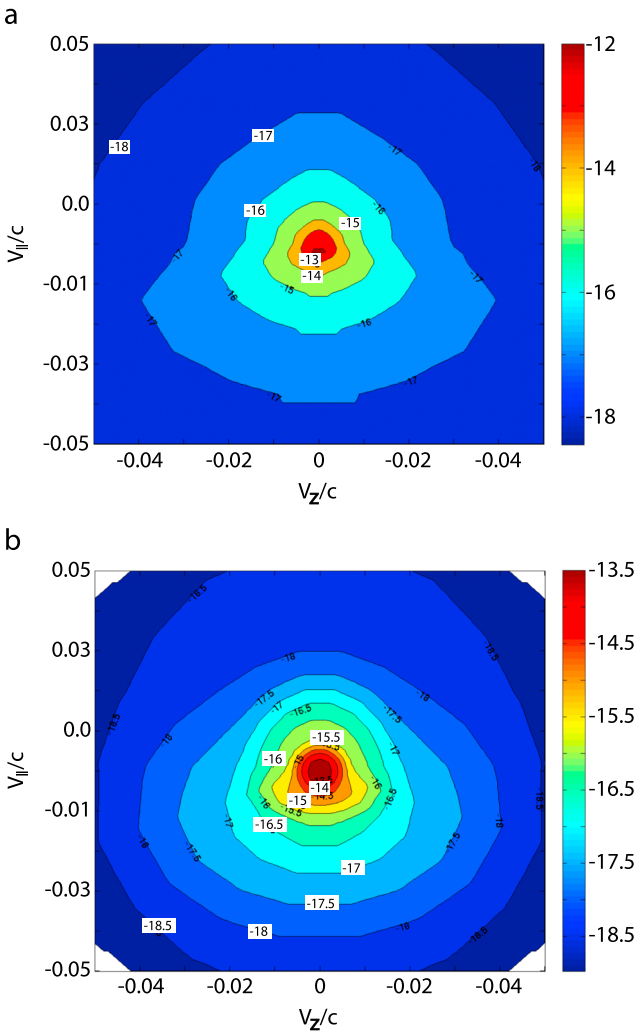

Figure 4. (a) Phase space density (PSD) after mirroring the data about the $V_{||}$ axis. The color bar units are log{PSD (s^3/m^6)}. For the anti-field-aligned direction note a distinct increase in electron particle flux and a temperature anisotropy. (b) Least squares fit model distribution using the data from Table 3.

$\chi^2 = 126$, 84, and 56, respectively. In Table 3 we list the plasma parameters (except for the density) for each population ($m = 5$) obtained from the fit and we include in parentheses the calculated percent relative uncertainty ($|\Delta p|/p$) of each variable parameter (p). The densities in Table 3 (column 1) are the values obtained by the least squares analysis divided by a factor of 6.2, as we now explain.

The density values in Table 3 are consistent with a plasma frequency of about 6 kHz, which is about a factor of 2.5 lower than interpreted from the data of Figure 4a, but we have good reason to believe that the actual density in the source region is less than that interpreted from the sampled CAPS/ELS electron distribution (Figure 4a), based on Langmuir Probe measurements (Figure 2b). The discrepancy may be due in part to the sampling periods, temporal variations of the local plasma, or spacecraft charging. During the time of the data shown in Figure 4a, the average density determined by the Langmuir Probe is 0.380 cm^{-3} corresponding to $f_{pe} = 5.53$ kHz (similar to Table 3). In addition, the polarization of the Z-mode emission at this time is left-handed, consistent with Z mode propagating at a frequency less than the plasma frequency [*Benson et al.*, 2006], but above the Z-mode cutoff, f_z.

A plot of the model distribution based on the data from Table 3 is shown in Figure 4b. We have made cuts of both the observed and model phase space distribution at pitch angles 109° and 168° as shown in Figure 5. The "plus" symbol designates the observed PSD, while the "cross" symbol is the model value. To produce the plots of Figures 4b and 5 the density used for each plasma population in Table 3 was multiplied by a factor of 6.2 (as discussed previously), while all the other parameters were the same. The fit to the data is good, but the model becomes increasingly too low at the largest velocities for $\alpha = 109°$. We address this problem later with the introduction of a kappa distribution

Table 3. Bi-Maxwellian Fit to Observations

Population	n (m^{-3})[a]	$w_{||}$(m/s)	$T_\perp/T_{||}$	V_{drft}(m/s)
Cool	2.97×10^5 (0.63)[b]	8.75×10^5 (0.29)	0.861 (0.56)	0.0
Warm 1	4.57×10^4 (0.89)	3.12×10^6 (0.37)	0.603 (0.81)	0.0
Warm 2	1.38×10^4 (0.71)	1.45×10^7 (0.59)	0.629 (0.94)	0.0
Drifting 1	6.27×10^4 (0.63)	1.02×10^6 (0.48)	4.40 (0.74)	1.5×10^6
Drifting 2	2.50×10^4 (0.63)	4.76×10^6 (0.39)	1.82 (0.70)	3.0×10^6

[a](Calculated value)/6.2.
[b]Percent uncertainty in parentheses.

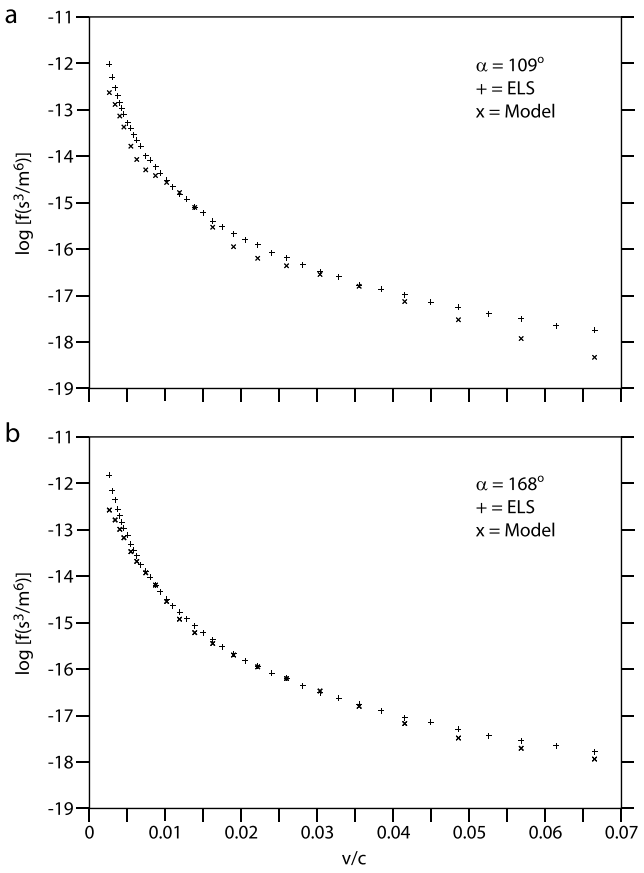

Figure 5. Cuts of the observed and model PSD at pitch angles (α) of (a) 109° and (b) 168° as labeled.

fit. Positive spacecraft charging at this time prevents analysis of $E \lesssim 2$ eV. There is no directly observed loss cone, but one might be conjectured assuming that electron scattering over the sampling period (4 s) may have obscured any loss cone present. At the time of the observations the spacecraft is at a latitude of ~28°. Assuming a magnetic mirror point of ~1.1 R_s, and using the zonal harmonic magnetic field model [*Connerney et al.*, 1982], we find that we might expect a loss cone of about 11°. This would be at the outer edge of the anode at 168° and may not be observed.

The general shape of the plasma distribution shown in Figures 4a and 4b (dominant plasma flux with a temperature anisotropy in the anti-field-aligned direction) is common throughout this time period of intense *Z*-mode emission. The primary changing parameter as a function of time is the plasma density which increases with time as the spacecraft approaches the magnetic equator and the ring plane [*Persoon et al.*, 2013]. As we show below, the growth of *Z* mode is limited by the ratio $\omega_{pe}/\Omega_{ce} < 0.35$, which thus limits the source location to times probably less than about 03:55.

3. Wave Growth Rate Analysis

3.1. Warm Plasma Analysis (Waves in Homogeneous Anisotropic Multicomponent Plasmas)

We investigate the growth of plasma waves based on the distribution model. We use the Waves in Homogeneous Anisotropic Multicomponent Plasmas (WHAMP) linear dispersion solver [*Rönnmark*, 1982, 1983] to search for unstable wave modes of the model distribution of Figure 4b. No nonlinear analysis is attempted. The dominant wave mode appears to be an electrostatic electron acoustic mode. The free energy source is the "Drifting 2" population, with both a temperature anisotropy and drift. Another source of the broad-banded electrostatic signatures is dust impacts near the ring plane [cf. *Kurth et al.*, 2006; *Wahlund et al.*, 2009; *Ye et al.*, 2014]. We will not discuss these effects further, but they are a part of the "background" emission in this region as Cassini approaches the Enceladus ring plane. We plot the resulting dispersion and growth rate curves in Figure 6, indicating a strong growth extending up and just beyond $f \sim f_{pe} = 5.97$ kHz. These waves are broad-banded with a peak growth rate near 5 kHz. An analytic expression for the electron acoustic mode for a two-component plasma is given as

$$\omega_{ea}^2 = \frac{\omega_{pc}^2}{1 + 1/k^2\lambda_{Dh}^2}\left(1 + 3k^2\lambda_{Dc}^2 + 3\frac{n_{0h}}{n_{0c}}\frac{T_c}{T_h}\right) \quad (2)$$

where λ_D, T, and n are the Deybe length, temperature, and density for the hot (h) and cold (c) plasma components, respectively, and k is the wave number [*Baumjohann and Treumann*, 2004, p. 264]. For comparison, in Figure 6 we have overplotted the electron acoustic dispersion curve obtained from equation (2) with

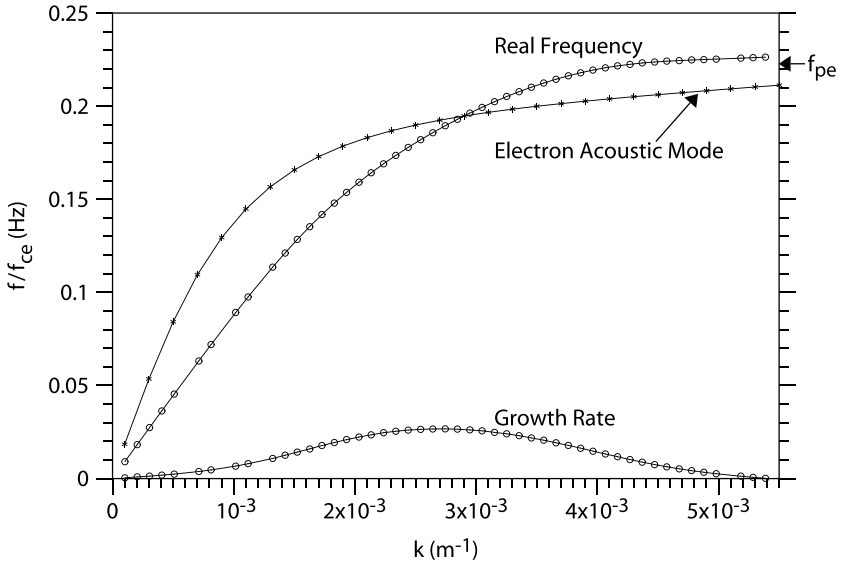

Figure 6. Dispersion and growth curves for the WHAMP analysis showing a broad spectrum with maximum growth near 5 kHz and damping near f_{pe}. These waves are reasonably narrow-banded with a peak near 5 kHz. The dispersion curve for the electron acoustic mode resulting from equation (2) is also plotted.

density and temperature parameters obtained from results from the "Cool" and Drifting 2 populations of Table 3. However, we have increased the density of the Cool population to maintain a plasma frequency of 5.97 kHz. The two dispersion curves have a similar shape, but the plasma distribution used in the WHAMP analysis may also support weak beam modes, and perhaps more than one electron acoustic mode.

For this modeled phase space distribution, a sum of bi-Maxwellians (Figure 4b), *Z* mode is not unstable. We proceed with a linear, cold plasma magnetoionic analysis by using a kappa distribution, which can better describe a high energy tail.

3.2. Kappa Distribution Analysis

Kappa distributions have been shown to be a powerful tool for representing suprathermal components that deviate from Maxwellian distributions [*Vasyliunas*, 1968; *Feldman et al*., 1975; *Gosling et al*., 1981; *Yoon et al*., 2013; *Yoon*, 2014]. The kappa model is numerically tractable and has numerous space plasma applications [cf. *Livadiotis and McComas*, 2013]. The phase space distribution shown in Figure 4a can also be modeled by using an isotropic Maxwellian distribution, f_0, and a combination of an isotropic kappa distribution and an electron conic (or weak loss cone) distribution. Electric conics are distributions enhanced just outside the loss cone [*Menietti and Burch*, 1985]. The kappa distribution allows for increased energy of the extended tail of the distribution compared to a Maxwellian. We proceed as follows:

$$f = f_0 + f_h, \tag{3}$$

$$f_0 = \frac{n_0}{\pi^{3/2} w_0^3} \exp\left(-\frac{v^2}{w_0^2}\right), \tag{4}$$

$$f_h = \frac{n_h}{\pi^{3/2}(\kappa w^2)^{3/2} A} \frac{\Gamma(\kappa+1)}{\Gamma(\kappa-1/2)} \frac{1}{(1+v^2/\kappa w^2)^{\kappa+1}} \left[1 - \tanh\frac{(\mu+\mu_0)^2}{\delta^2} + \Delta\left(1+\tanh\frac{\mu+\mu_0}{\delta}\right)\right], \tag{5}$$

$$A = \frac{1}{2}\int_{-1}^{1} d\mu \left[1 - \tanh\frac{(\mu+\mu_0)^2}{\delta^2} + \Delta\left(1+\tanh\frac{\mu+\mu_0}{\delta}\right)\right], \tag{6}$$

where f_0 is the cool distribution, f_h is the warm distribution, v is electron kinetic speed, w_0 is drift velocity, $\mu = \cos(\alpha)$ (α is the electron pitch angle), and $\Gamma(\kappa+1)$ is the gamma or factorial function. We choose the fitting parameters listed in Table 4.

The resulting phase space distribution is shown in Figure 7. A cut of the phase space distribution for the kappa distribution at a pitch angle of 109° is shown compared to the observations in Figure 7b. The Kappa

Table 4. Kappa Fit Parameters

w_o (m/s)	n_h (m^{-3})	μ_0	δ	Δ	κ
1.02×10^6	4.42×10^5	0.1	0.6	0.3	1

model density is multiplied by the same factor of 6.2 as explained above for Figure 5. The Kappa distribution fits better at higher velocities compared to the bi-Maxwellian distribution. An analysis of this distribution proceeds according to linear magnetoionic wave dispersion theory as presented in *Yoon et al.* [1996, 1998] and briefly summarized here. The wave dispersion relation for extraordinary (*X*), *Z*, and whistler (*W*) modes can be written as

$$N^2_{X/Z} = 1 - \frac{f^2_{pe}}{f(f+\tau f_{ce})},\ N^2_{W/O} = 1 - \frac{\tau f^2_{pe}}{f(\tau f - f_{ce}\cos^2\theta)}, \tag{7}$$

$$\tau = \left(s + \sqrt{s^2+\cos^2\theta}\right)\frac{f^2_{pe}-f^2}{\left|f^2_{pe}-f^2\right|},\ s = \frac{f f_{ce}\sin^2\theta}{2\left|f^2_{pe}-f^2\right|}, \tag{8}$$

where the various mode designations follow the customary practice based upon the range of wave frequency,

$$X \text{ mode}: f > f_X,\ Z \text{ mode}: f_Z < f < f^{res}_Z, \tag{9}$$

$$O \text{ mode}: f > f_{pe},\ W \text{ mode}: 0 < f < f^{res}_W, \tag{10}$$

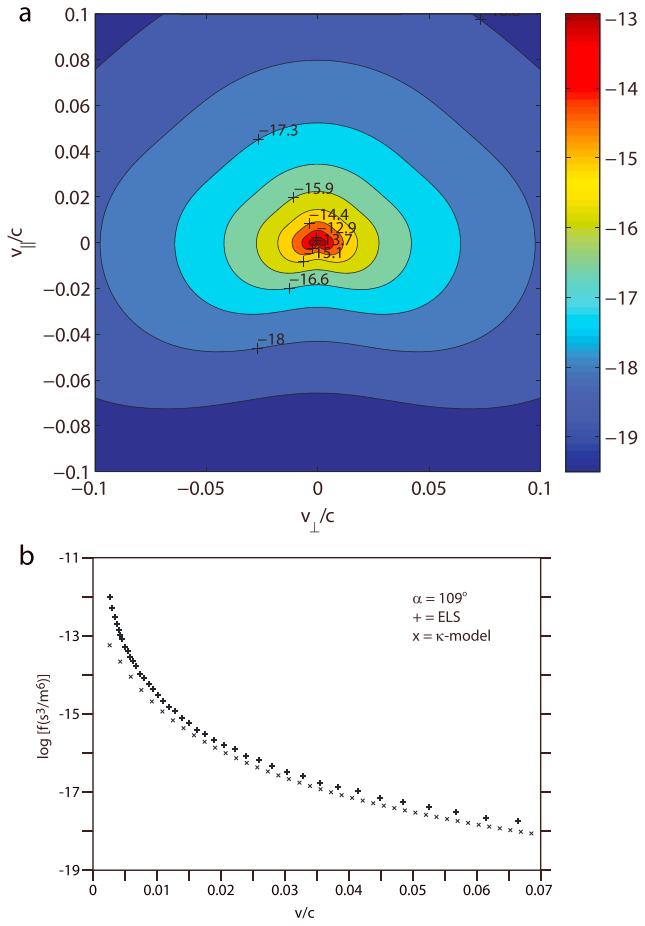

Figure 7. (a) Phase space distribution using a combination of an isotropic kappa distribution and an electron conic (or weak loss cone) distribution. Parameters are listed in Table 4. (b) Cuts of the observed and model PSD at pitch angle $\alpha = 109°$ for the kappa distribution as labeled. Note the better fit at larger velocities compared to the bi-Maxwellian fit of Figure 5 for the same pitch angle.

and where the various cutoffs and resonance frequencies are defined by

$$f_x = \frac{1}{2}\left(\sqrt{f_{ce}^2 + 4f_{pe}^2} + f_{ce}\right), \tag{11}$$

$$f_Z^{\mathrm{res}} = \frac{1}{\sqrt{2}}\left[f_{pe}^2 + f_{ce}^2 + \sqrt{\left(f_{pe}^2 - f_{ce}^2\right)^2 + 4f_{pe}^2 f_{ce}^2 \sin^2\theta}\right]^{1/2}, \tag{12}$$

$$f_W^{\mathrm{res}} = \frac{1}{\sqrt{2}}\left[f_{pe}^2 + f_{ce}^2 - \sqrt{\left(f_{pe}^2 - f_{ce}^2\right)^2 + 4f_{pe}^2 f_{ce}^2 \sin^2\theta}\right]^{1/2}, \tag{13}$$

and f_z was given previously in section 1.

The temporal growth rate is then expressed as

$$\gamma_\sigma = \frac{f_{pe}^2}{f}\frac{\pi^2}{R_\sigma}\sum_{s=0}^{\infty}\left(\Theta(sf_{ce} - f)\int_{-1}^{1} d\mu Q_s^\sigma(u_+, \mu) + \Theta(f - sf_{ce})\Theta\left(1 - \mu_s^2\right)\int_{\mu_s}^{1} d\mu \sum_{+,-} Q_s^\sigma(u_\pm, \mu)\right), \tag{14}$$

where σ stands for X, Z, W, or O, and

$$Q_s^{X/Z}(u,\mu) = \frac{\tau^2}{\tau^2 + \cos^2\theta}\frac{u^2(1-\mu^2)}{\left|u - N_{X/Z}\mu\cos\theta\right|}\left[\frac{f}{f_{ce}}\left(K_{X/Z}\sin\theta + \frac{\cos\theta}{\tau}\left(\cos\theta - N_{X/Z}u\mu\right)\right)\right.$$
$$\left.\times\frac{J_s(b)}{b} + J'_s(b)\right]^2\left(u\frac{\partial}{\partial u} + \left(N_{X/Z}u\cos\theta - \mu\right)\frac{\partial}{\partial\mu}\right)f(u,\mu), \tag{15}$$

$$Q_s^{W/O}(u,\mu) = \frac{1}{\tau^2 + \cos^2\theta}\frac{u^2(1-\mu^2)}{\left|u - N_{W/O}\mu\cos\theta\right|}\left[\frac{f}{f_{ce}}\left(K_{W/O}\sin\theta\cos\theta - \tau\left(\cos\theta - N_{W/O}u\mu\right)\right)\right.$$
$$\left.\times\frac{J_s(b)}{b} + \cos\theta J'_s(b)\right]^2\left(u\frac{\partial}{\partial u} + \left(N_{W/O}u\cos\theta - \mu\right)\frac{\partial}{\partial\mu}\right)f(u,\mu), \tag{16}$$

$$u_\pm = N_\sigma\mu\cos\theta \pm \sqrt{N_\sigma^2\mu^2\cos^2\theta + 2\left(\frac{sf_{ce}}{f} - 1\right)}, \tag{17}$$

$$\mu_s = \frac{\sqrt{2}}{N_\sigma\cos\theta}\left(1 - \frac{sf_{ce}}{f}\right)^{1/2}, \quad b = \frac{f}{f_{ce}}N_\sigma u_\pm\sqrt{1-\mu^2}\sin\theta, \tag{18}$$

$$K_{X/Z} = \frac{f_{pe}^2}{f_{pe}^2 - f^2}\frac{f_{ce}\sin\theta}{f + \tau f_{ce}}, \quad K_{W/O} = \frac{f_{pe}^2}{f_{pe}^2 - f^2}\frac{\tau f_{ce}\sin\theta}{\tau f - f_{ce}\cos^2\theta}. \tag{19}$$

For the kappa-loss-cone distribution the quantity of interest is

$$u\frac{\partial f}{\partial u} + \left(N_\sigma u\cos\theta - \mu\right)\frac{\partial f}{\partial\mu} = -\frac{n_h}{\pi^{3/2}\left(\kappa w^2\right)^{3/2}A}\frac{\Gamma(\kappa+1)}{\Gamma(\kappa - 1/2)}$$
$$\times\left\{\frac{2u^2}{w^2}\frac{\kappa+1}{\kappa}\frac{1}{\left(1 + v^2/\kappa w^2\right)^{\kappa+2}}\left[1 - \tanh\frac{(\mu+\mu_0)^2}{\delta^2} + \Delta\left(1 + \tanh\frac{\mu+\mu_0}{\delta}\right)\right]\right. \tag{20}$$
$$\left.+\frac{1}{\left(1 + v^2/\kappa w^2\right)^{\kappa+1}}\frac{N_\sigma u\cos\theta - \mu}{\delta}\left(\frac{2(\mu+\mu_0)}{\delta}\mathrm{sech}^2\frac{(\mu+\mu_0)^2}{\delta^2} - \Delta\,\mathrm{sech}^2\frac{\mu+\mu_0}{\delta}\right)\right\}.$$

The growth rate superimposed on top of the dispersion surface is shown for both Z and W modes in Figure 8 a. The individual surfaces are shown in Figures 8b and 8c, respectively. The free energy source of the Z-mode and whistler mode emission is the temperature anisotropy. Note that the W mode is unstable for $\omega/\Omega_e \sim 0.05$ ($f \sim 1.5$ kHz) for quasi-parallel propagation angles in a narrow range of frequencies. In contrast, the Z mode is unstable for quasi-parallel directions over a broader range of frequencies closer to ω_{pe}. In Figure 9 we show the calculated growth rate as a function of frequency for three values of wave normal angle, θ, i.e., the angle between the wave vector, **k**, and the magnetic field. The Z-mode growth ranges from ~2 kHz to ~4.5 kHz for $\Gamma > 4.5 \times 10^{-4}$ kHz at wave normal angle near zero. The calculated Z-mode growth could explain the intense (red) emission of Figure 2b (03:15 to 04:30) and the possible whistler mode emission (green) observed at lower frequencies in the same time interval.

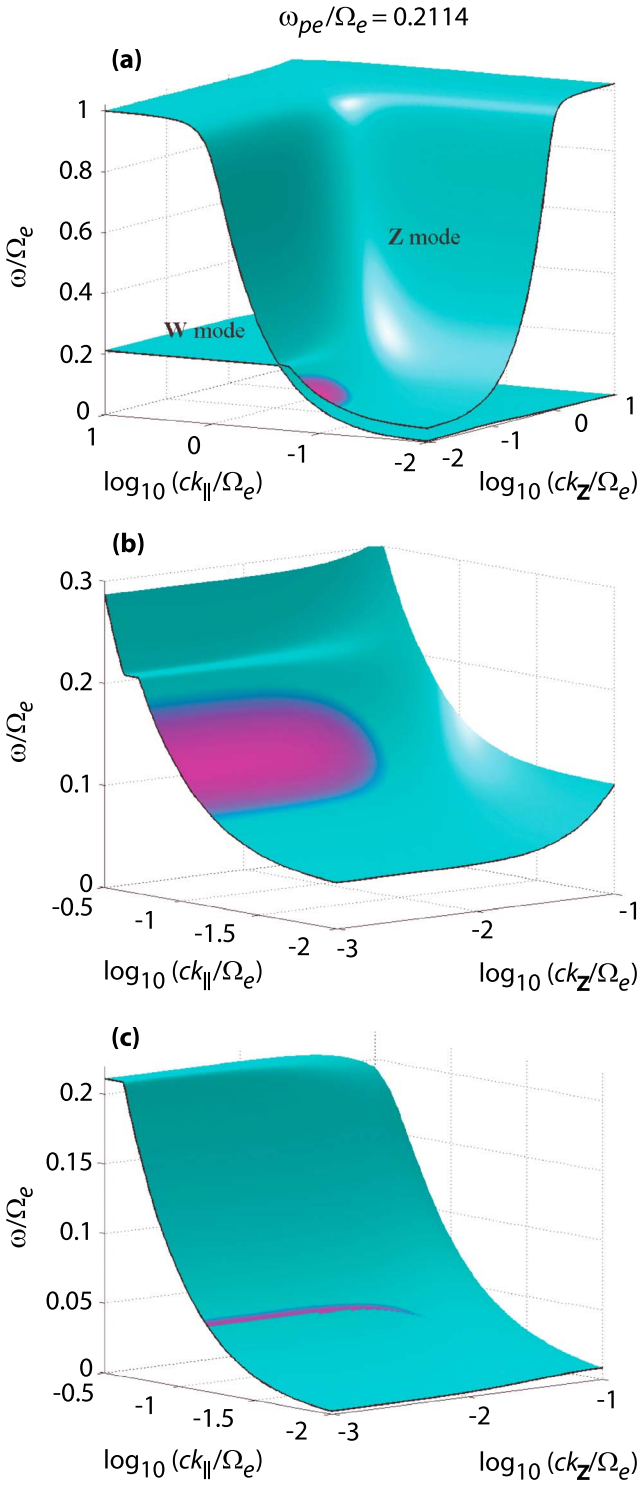

Figure 8. We choose $\omega_{pe}/\Omega_e = 0.2144$ corresponding to $f_{pe} = 6$ kHz and obtain the dispersion surfaces shown in Figure 8a. Growth rate superimposed on top of the dispersion surface is shown for both *Z* and *W* modes in Figures 7b and 7c, respectively.

The expected gain of the *Z*-mode emission can be estimated and is dependent on the radiation background levels. Some of the weakest observations of *Z*-mode emission during this event are seen earlier on the same day near 02:22 and within the frequency range of $4\,\text{kHz} < f < 5\,\text{kHz}$ with spectral density $\sim 2\times10^{-13}\,\text{V}^2\,\text{m}^2\,\text{Hz}^{-1}$. For typical values of *Z* mode during the most intense emission, spectral densities are $\sim 5\times10^{-10}\,\text{V}^2\,\text{m}^2\,\text{Hz}^{-1}$, therefore

$$G = I/I_o \sim 5\times10^{-10}/2\times10^{-13} = 2.5\times10^3 \quad (21)$$

$$G = \exp(2\,\Gamma\tau_g) = 2.5\times10^3, \quad (22)$$

where Γ is the temporal growth rate of the wave amplitude and τ_g is the growth time.

$$2\Gamma\tau_g = 7.8, \quad \tau_g \sim 4s \quad (23)$$

We suspect that the phase space distribution we observe is relaxed from that which actually generated the waves, and thus, the growth rate predicted from the measured distributions is smaller.

The whistler mode growth is quite weak and for a very narrow range of frequencies near 2 kHz. This is reasonably consistent with the observations, which show only weak whistler mode emission for $f < 3.5$ kHz.

We have investigated the growth rate of *Z* mode at higher plasma densities, but at $\omega_{pe}/\Omega_{ce} > 0.35$ the *Z* mode is damped except for cyclotron-maser emission near Ω_{ce}. We believe that our choice of $\omega_{pe}/\Omega_{ce} = 0.21$ is reasonable, based on Langmuir Probe measurements and the temporal nature of the plasma population. The polarization of the *Z*-mode emission between 03:30 to 04:00 is left-handed, indicating that the *Z* mode is propagating in a region where $\omega < \omega_{pe}$, consistent with our choice of f_{pe} ~6 kHz.

4. Summary and Conclusion

We have conducted a survey of possible source regions of 5 kHz narrowband *Z*-mode emission in the Saturn lower density region of the inner magnetosphere. Six such regions were chosen for further study, but only one region provided marginally sufficient sampling of electron pitch angles for determination of the phase space distribution. We have introduced two electron distributions. The first is a

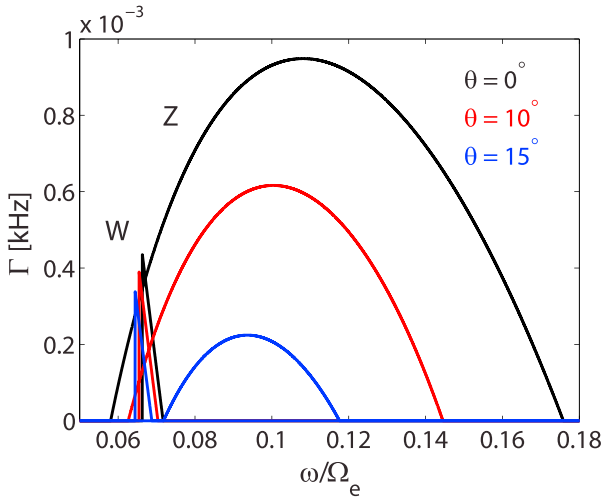

Figure 9. Temporal growth rate as a function of frequency for three wave normal angles.

least squares fit of the available PSD to a sum of bi-Maxwellians. This distribution contains no loss cone because none is directly observable possibly due to the limited coverage of the ELS anodes near the field-aligned direction and the 4 s sampling period. An analysis of this distribution with the WHAMP dispersion solver finds growth of electron acoustic waves but not of *Z*-mode waves. We then introduce a kappa distribution with a weak loss cone that is consistent with the data because of the observational uncertainties. For this distribution linear cold plasma magnetoionic theory [*Yoon et al*., 1996, 1998] is applied to discover wave growth for the *Z* mode. We have identified a probable free energy source for the growth of *Z* mode as a temperature anisotropy and a weak loss cone. The frequency range of the *Z* mode is calculated to be approximately 2–5 kHz compared to the observed range of about 3–7 kHz, with the maximum frequency dependent on the plasma frequency of the source population. The modeled *Z*-mode growth rates are adequate to explain the observations with caveats. Whistler mode emission is also calculated to grow weakly in a narrow frequency range of a few hundred Hz near 2 kHz. Consistent with this, only weak whistler mode emission is observed for $f < 3.5$ kHz.

The region of the probable source, the inner edge of the Enceladus density torus, and near magnetic field lines that map to the radiation belt can saturate some ELS anode measurements, and in the present case there are also anode obscuration difficulties. In addition, data are sampled over two distinct 4 s periods separated by approximately 3.5 min. These problems make the task of obtaining a sufficient electron phase space distribution very challenging. However, the time history of the event (cf. Figure 3) indicates a general pattern of consistently dominant electron phase space density in the anti-field-aligned direction. This provides confidence in the assumption of relatively constant PSD levels during the ~3.5 min separating the two sets of electron data (Sets A and B). The results suggest that narrowband emission, often observed in a frequency range centered near 5 kHz, can be generated by sources in the outer edge of the Enceladus torus, where the conditions $\omega_{pe}/\Omega_{ce} \lesssim 0.3$, $T_\perp/T_\parallel > 1$, and a weak loss cone are sufficient to support growth of the *Z* mode. A source of temperature anisotropy near the Enceladus torus may be damping of ion cyclotron waves which have been identified and studied by many researchers [cf. *Leisner et al*., 2006; *Menietti et al*., 2013]. The narrow size of the source location may be due to the steep gradient in the density in this inner region of the Saturn magnetosphere. For the region of *Z*-mode growth analyzed in this work, the plasma $\beta \ll 1$. But as β increases nearer to the magnetic equator and the ring plane cyclotron and Landau damping of the *Z*-mode increase [cf. *Gary*, 1993], broadband electrostatic emission also increases in amplitude coincident with the onset of the intense *Z*-mode emission at ~03:15. The broadband emission is partially due to the electron acoustic mode (and possibly weak beam modes) generated by the observed plasma distribution, and probably also to the presence of dust impacts on the spacecraft antennas.

These studies provide a reasonable explanation for the presence of *Z*-mode emission in the inner magnetosphere of Saturn. Damping of and wave-particle interactions with this emission is a probable source of electron acceleration of electrons as suggested by *Horne and Thorne* [1998] for Earth, and *Gu et al*. [2013] and *Menietti et al*. [2015] for Saturn and should be the subject of further investigations.

Acknowledgments
We wish to thank J. Barnholdt for clerical assistance and J. Chrisinger for help with several figures. J.D.M. acknowledges support from NASA grant NNX11AM36G. In addition, J.D.M., D.P., and S.-I.Y. acknowledge support from JPL contract 1415150. Cassini RPWS data are archived in calibrated, full resolution at the NASA Planetary Data System website: http//pds.nasa.gov/ds-view/pdsviewDataset.jsp?dsid=CO-V/E/J/s/SS-RPWS-3-RDR-LRFULL-V1.0. Observations of the CAPS/ELS instrument and the magnetic field instrument MAG on Cassini are available at http://ppi.pds.nasa.gov. P.H.Y. acknowledges NSF grant AGS1550566 to the University of Maryland and the support by the BK21 plus program through the National Research Foundation funded by the Ministry of Education of Korea, to Kyung Hee University, Korea. He also acknowledges the Science Award Grant from the GFT Foundation to the University of Maryland. O.S. acknowledges support from the LH14010 grant and from the Praemium Academiae award.

References

Albert, J. M. (2007), Refractive index and wavenumber properties for cyclotron resonant quasilinear diffusion by cold plasma waves, *Phys. Plasmas*, *14*, 072901, doi:10.1063/1.2744363.

Arridge, C. S., L. K. Gilbert, G. R. Lewis, E. C. Sittler, G. H. Jones, D. O. Kataria, A. J. Coates, and D. T. Young (2009), The effect of spacecraft radiation sources on electron moments from the Cassini CAPS electron spectrometer, *Plan. Space Sci.*, *57*, 854–868, doi:10.1016/j.pss.2009.02.011.

Baumjohann, W., and R. A. Treumann (2004), *Basic Space Plasma Physics*, p. 264, Imperial College Press, London.
Benson, R. F., P. A. Webb, J. L. Green, D. L. Carpenter, V. S. Sonwalkar, H. G. James, and B. W. Reinisch (2006), Active wave experiments in space plasmas: The Z Mode, in *Geospace Electromagnetic Waves and Radiation*, edited by J. W. LaBelle and R. A. Treumann, pp. 3–35, Springer, Berlin, doi:10.1007/3-540-33203-0_1.
Bevington, P. R. (1969), *Data Reduction and Error Analysis for the Physical Sciences*, pp. 235–242, McGraw-Hill Book Company, New York.
Coates, A. J., C. Alsop, A. J. Coker, D. R. Linder, A. J. Johnstone, R. D. Woodliffe, M. Grande, A. Preece, S. Burge, and D. S. Hall (1996), The electron spectrometer for the Cassini spacecraft, *J. Br. Interplanet. Soc.*, *45*(9), 387–392.
Connerney, J. E. P., N. F. Ness, and M. H. Acuna (1982), Zonal harmonic model of Saturn's magnetic field from Voyager 1 and 2 observations, *Nature*, *298*, 44–46, doi:10.1038/298044a0.
Dougherty, M. K., et al. (2004), The Cassini magnetic field investigation, *Space Sci. Rev.*, *114*, 331–383, doi:10.1007/s11214-004-1432-2.
Feldman, W. C., J. R. Asbridge, S. J. Bame, M. D. Montgomery, and S. P. Gary (1975), Solar wind electrons, *J. Geophys. Res.*, *80*(31), 4181–4196, doi:10.1029/JA080i031p04181.
Gary, S. P. (1993), *Theory of Space Plasma Microinstabilities*, *Cambridge Atmos. Space Sci. Ser.*, pp. 112–116, Cambridge Univ. Press, New York.
Glauert, S. A., and R. B. Horne (2005), Calculation of pitch angle and energy diffusion coefficients with the PADIE code, *J. Geophys. Res.*, *110*, A04206, doi:10.1029/2004JA010851.
Gosling, J. T., J. R. Asbridge, S. J. Bame, W. C. Feldman, R. D. Zwickl, G. Paschmann, N. Sckopke, and R. J. Hynds (1981), Interplanetary ions during an energetic storm particle event: The distribution function from solar wind thermal energies to 1.6 MeV, *J. Geophys. Res.*, *86*(A2), 547–554, doi:10.1029/JA086iA02p00547.
Gu, X., R. M. Thorne, B. Ni, and S.-Y. Ye (2013), Resonant diffusion of energetic electrons by narrowband Z mode waves in Saturn's inner magnetosphere, *Geophys. Res. Lett.*, *40*, 255–261, doi:10.1029/2012GL054330.
Gurnett, D. A., and A. Bhattacharjee (2005), *Introduction to Plasma Physics*, Cambridge Univ. Press, Cambridge, p. 124, doi:10.1017/CBO9780511809125.
Gurnett, D. A., S. D. Shawhan, and R. R. Shaw (1983), Auroral hiss, Z-mode radiation, and auroral kilometric radiation in the polar magnetosphere: DE 1 observations, *J. Geophys. Res.*, *88*(A1), 329–340, doi:10.1029/JA088iA01p00329.
Gurnett, D. A., et al. (2004), The Cassini radio and plasma wave investigation, *Space Sci. Rev.*, *114*, 395–463, doi:10.1007/s11214-004-1434-0.
Horne, R. B., and R. M. Thorne (1998), Potential waves for relativistic electron scattering and stochastic acceleration during magnetic storms, *Geophys. Res. Lett.*, *25*(15), 3011–3014, doi:10.1029/98GL01002.
Kurth, W. S. (1982), Detailed observations of the source of terrestrial narrowband electromagnetic radiation, *Geophys. Res. Lett.*, *9*, 1341–1344, doi:10.1029/GL009i012p01341.
Kurth, W. S., T. F. Averkamp, D. A. Gurnett, and Z. Wang (2006), Cassini RPWS observations of dust in Saturn's E Ring, *Plan. Space Sci.*, *54*, 988–998, doi:10.1016/j.pss.2006.05.011.
Leisner, J. S., C. T. Russell, M. K. Dougherty, X. Blanco-Cano, R. J. Strangeway, and C. Bertucci (2006), Ion cyclotron waves in Saturn's E ring: Initial Cassin observations, *Geophys. Res. Lett.*, *33*, L11101, doi:10.1029/2005GL024875.
Livadiotis, G., and D. J. McComas (2013), Understanding kappa distributions: A toolbox for space science and astrophysics, *Space Sci. Rev.*, *175*, 183–214, doi:10.1007/s11214-013-9982-9.
Menietti, J. D., and J. L. Burch (1985), Electron Conic" signatures observed in the nightside auroral zone and over the polar cap, *J. Geophys. Res.*, *90*(A6), 5345–5353, doi:10.1029/JA090iA06p05345.
Menietti, J. D., and P. H. Yoon (2006), Plasma waves and fine structure emission bands within a plasmapause density cavity source region, *Geophys. Res. Lett.*, *33*, L15101, doi:10.1029/2005GL025610.
Menietti, J. D., R. L. Mutel, P. Schippers, S.-Y. Ye, D. A. Gurnett, and L. Lamy (2011), Analysis of Saturn kilometric radiation near a source center, *J. Geophys. Res.*, *116*, A12222, doi:10.1029/2011JA017056.
Menietti, J. D., P. Schippers, Y. Katoh, J. S. Leiser, G. B. Hospodarsky, D. A. Gurnett, and O. Santolik (2013), Saturn chorus intensity variations, *J. Geophys. Res. Space Physics*, *118*, 5592–5602, doi:10.1002/jgra.50529.
Menietti, J. D., T. F. Averkamp, J. B. Groene, R. B. Horne, Y. Y. Shprits, E. E. Woodfield, G. B. Hospodarsky, and D. A. Gurnett (2014), Survey analysis of chorus intensity at Saturn, *J. Geophys. Res. Space Physics*, *119*, 8415–8425, doi:10.1002/2014JA020523.
Menietti, J. D., T. F. Averkamp, S.-Y. Ye, R. B. Horne, E. E. Woodfield, Y. Y. Shprits, D. A. Gurnett, A. M. Persoon, and J.-E. Wahlund (2015), Survey of Saturn Z-mode emission, *J. Geophys. Res. Space Physics*, *120*, 6176–6187, doi:10.1002/2015JA021426.
Persoon, A. M., D. A. Gurnett, J. S. Leisner, W. S. Kurth, J. B. Groene, and J. B. Faden (2013), The plasma density distribution in the inner region of Saturn's magnetosphere, *J. Geophys. Res. Space Physics*, *118*, 2970–2974, doi:10.1002/jgra.50182.
Rönnmark, K. (1982), WHAMP waves in a homogeneous anisotropic multi-component plasma Rep. 179, Kiruna Geophys. Inst., Kiruna, Sweden.
Rönnmark, K. (1983), Computation of the dielectric tensor of a Maxwellian plasma, *Plasma Phys.*, *25*(6), 699–701, doi:10.1088/0032-1028/25/6/007.
Shprits, Y. Y., J. D. Menietti, X. Gu, K. C. Kim, and R. B. Horne (2012), Gyroresonant interactions between the radiation belt electrons and whistler mode chorus waves in the radiation environments of Earth, Jupiter, and Saturn: A comparative study, *J. Geophys. Res.*, *117*, A11216, doi:10.1029/2012JA018031.
Vasyliunas, V. M. (1968), A survey of low-energy electrons in the evening sector of the magnetosphere with OGO 1 and OGO 3, *J. Geophys. Res.*, *73*(9), 2839–2884, doi:10.1029/JA073i009p02839.
Wahlund, J.-E., et al. (2005), The inner magnetosphere of Saturn: Cassini RPWS cold plasma results from the first encounter, *Geophys Res. Lett.*, *32*, L20509, doi:10.1029/2005GL022699.
Wahlund, J.-E., et al. (2009), Detection of dusty plasma near the E-ring of Saturn, *Plan. Space Sci.*, *57*, 1795–1806, doi:10.1016/j.pss.2009.03.011.
Xiao, F., S. Zhang, Z. Su, Z. He, and L. Tang (2012), Rapid acceleration of radiation belt energetic electrons by Z-mode waves, *Geophys. Res. Lett.*, *39*, L03103, doi:10.1029/2011GL050625.
Ye, S.-Y., J. D. Menietti, G. Fischer, Z. Wang, B. Cecconi, D. A. Gurnett, and W. S. Kurth (2010), Z mode waves as the source of Saturn narrowband radio emissions, *J. Geophys. Res.*, *115*, A08228, doi:10.1029/2009JA015167.
Ye, S.-Y., D. A. Gurnett, W. S. Kurth, T. F. Averkamp, M. Morooka, S. Sakai, and J.-E. Wahlund (2014), Electron density inside Enceladus plume inferred from plasma oscillations excited by dust impacts, *J. Geophys. Res. Space Physics*, *119*, 3373–3380, doi:10.1002/2014JA019861.
Yoon, P. H. (2014), Electron kappa distribution and quasi-thermal noise, *J. Geophys. Res. Space Physics*, *119*, 7074–7087, doi:10.1002/2014JA020353.
Yoon, P. H., A. T. Weatherwax, T. J. Rosenberg, and J. LaBelle (1996), Lower ionospheric cyclotron maser theory: A possible source of $2f_{ce}$ and $3f_{ce}$ auroral radio emissions, *J. Geophys. Res.*, *101*(A12), 27,015–27,025, doi:10.1029/96JA02664.

Yoon, P. H., A. T. Weatherwax, and T. J. Rosenberg (1998), On the generation of auroral radio emissions at harmonics of the lower ionospheric electron cyclotron frequency: X, O and Z mode maser calculations, *J. Geophys. Res.*, *103*(A3), 4071–4078, doi:10.1029/97JA03526.

Yoon, P. H., L. F. Ziebell, R. Gaelzer, L. Wang, and R. P. Lin (2013), Solar wind electron acceleration via Langmuir turbulence, *Terr. Atmos. Ocean. Sci.*, *24*, 175–182, doi:10.3319/TAO.2012.05.30.01(SEC).

Young, D. T., et al. (2004), Cassini plasma spectrometer investigation, *Space Sci. Rev.*, *114*, 1–112, doi:10.1007/s11214-004-1406-4.